



# A computational insight on the aromatic amino acids conjugation with $[\text{Cp}^*\text{Rh}(\text{H}_2\text{O})_3]^{2+}$ by using the meta-dynamics/FMO3 approach

Roberto Paciotti<sup>1</sup> · Alessandro Marrone<sup>1</sup>

Received: 13 October 2023 / Accepted: 23 November 2023 / Published online: 12 December 2023  
© The Author(s) 2023

## Abstract

**Context** Rh(III) complexes demonstrated to exert promising pharmacological effects with potential applications as anti-cancer, anti-bacterial, and antimicrobial agents. One important Rh(III)-ligand is the pentamethylcyclopentadienyl ( $\text{Cp}^*$ ) group forming in water the  $[\text{Cp}^*\text{Rh}(\text{H}_2\text{O})_3]^{2+}$  complex. Among of its attractive chemical properties is the ability to react specifically with Tyr amino acid side chain of G-protein-coupled receptor (GPCR) peptides by means of highly chemoselective bioconjugation reaction, at room temperature and at pH 5–6. In this computational work, in order to deepen the mechanism of this chemoselective conjugation, we study the ligand exchange reaction between  $[\text{Cp}^*\text{Rh}(\text{H}_2\text{O})_3]^{2+}$  and three small molecules, namely *p*-cresol, 3-methylimidazole, and toluene, selected as mimetic of aromatic side chains of tyrosine (Tyr), tryptophan (Trp) and phenylalanine (Phe), respectively. Our outcomes suggest that the high selectivity for Tyr side chain might be related to OH group able to affect both thermodynamic and kinetic of ligand exchange reaction, due to its ability to act as both H bond acceptor and donor. These mechanistic aspects can be used to design new metal drugs containing the  $[\text{Cp}^*\text{Rh}]^{2+}$  scaffold targeting specifically Tyr residues involved in biological/pathological processes such as phosphorylation by means of Tyr-kinase enzyme and protein–protein interactions.

**Methods** The geometry of three encounter complexes and product adducts were optimized at the B3LYP//CPCM/ $\omega$ B97X-D level of theory, adopting the 6-311+G(d,p) basis set for all non-metal atoms and the LANL2DZ pseudopotential for the Rh atom. Meta-dynamics RMSD (MTD(RMSD)) calculations at GFN2-xTB level of theory were performed in NVT conditions at 298.15 K to investigate the bioconjugation reactions (simulation time: 100 ps; integration step 2.0; implicit solvent model: GBSA). The MTD(RMSD) simulation was performed in two replicates for each encounter complex. Final representative subsets of 100 structures for each run were gained with a sampling rate of 1 ps and analyzed by performing single point calculations using the FMO3 method at RI-MP2/6-311G//PCM[1] level of theory, adopting the MCP-TZP core potential for Rh atom.

**Keywords** FMO3 · Pair interaction energy · MTD · Meta-dynamics · Metal-based drugs ·  $[\text{Cp}^*\text{Rh}]^{2+}$

## Introduction

The vast chemical complexity of biological systems is probably the most challenging aspect to deal with in the development of new therapeutics. Indeed, the capability of exerting an atomistic control of the structure and function of biomolecular systems via the administration of active compounds is often hampered by the lack of an adequate chemical and/or compartmental/tissue selectivity.

In this frame, the high toxicity disclosed by metal-based drugs can be often ascribed to their high and multifacet reactivity inducing an uncontrolled multi-target or multi-organ response instead of specific therapeutic activity.

Since the discovery of cisplatin, CP [1], the search for new effective metal drugs is a never-ending race. The anticancer activity of this prominent metallodrug is ascribed to the binding at consecutive purine nucleobases by causing so-called 1,2-intrastrand lesions. Nevertheless, together with its derivatives (carboplatin and oxaliplatin), CP lasts as the most used metal drug for the treatment of several solid tumors [2, 3], in spite of its nephrotoxicity and chemoresistance [4, 5].

✉ Roberto Paciotti  
r.paciotti@unich.it

<sup>1</sup> Department of Pharmacy, Università “G. D’Annunzio” Di Chieti-Pescara, I-66100 Chieti, Italy

As a consequence, several efforts were performed to discover new classes of metal-drugs containing other metals such as Au, Ti, Ru, Re, Ga, Ir, Rh, and others [6–8].

Among them, Rh(III) complexes, compared with the typical square planar Pt(II) complexes, is characterized by structural diversity which is considered as a potential advantage of this metal ion which leads to the different modes of interaction of these complexes with biomolecular targets [9]. They have shown several pharmaceutical applications such as anti-cancer, anti-bacterial, and antimicrobial activity acting as protein binders or modulating protein–protein interactions (PPIs) [9]. Notably, Rh-containing complexes can be used not only for therapeutic applications but also as luminescent probes or labels for biomolecules [10].

Due to these important pharmacological properties, Rh-containing compounds were deeply studied and many complexes were designed with promising in vitro efficacy [11, 12] although none of them have reached the market.

One important Rh(III)-ligand is the pentamethylcyclopentadienyl (Cp\*) group since it gives favorable chemical properties to the corresponding metal complexes such as a good solubility and stability [13]. Due to these important features, [Cp\*Rh]<sup>2+</sup> complexes have widely applied in catalysis [14, 15] and in coordination chemistry.

Many Rh(III) complexes containing Cp\* were designed to act as isomerase inhibitors demonstrated promising in vitro activity [9]. [Cp\*Rh]<sup>2+</sup> scaffold is also included in metal compound, such as [Cp\*Rh(Ph<sub>3</sub>P)Cl<sub>2</sub>], which act as protease inhibitors with potential therapeutic use for the treatment of diseases such as cancers, fungal and viral infections, Alzheimer's disease, and inflammatory disorders [9]. Interestingly, the [Cp\*Rh]<sup>2+</sup> complexes were also investigated as possible vehicles to deliver anti-cancer drugs, such as curcumin, to the tumor cells [16].

In water the [Cp\*Rh]<sup>2+</sup> complexes is found in the hydrated form, [Cp\*Rh(H<sub>2</sub>O)<sub>3</sub>]<sup>2+</sup>. It is able to react specifically with Tyr amino acid side chain of G-protein–coupled receptor (GPCR) peptides, as [Tyr<sup>1</sup>]-Leu-enkephalin, [Tyr<sup>4</sup>]-neurotensin (8-13), and [Tyr<sup>3</sup>]-octreotide, by means of highly chemoselective bioconjugation reaction, at room temperature and at pH 5-6 [17, 18]. In a recent computational study, performed using classical molecular dynamics (MD) and density functional theory (DFT) methods, we analyzed the effect of Tyr conjugation reactions on protein conformations of the above-mentioned GPCR peptides [19]. Moreover, we found that the mesomeric e-donating (+M) effect of the Tyr phenol OH group provides high thermodynamic stability to [Cp\*Rh(Tyr-peptide)]<sup>2+</sup> complex, representing the mechanistic rationale for this chemoselective reaction.

In this work, in order to deepen the mechanism of this chemoselective conjugation we study the ligand exchange reaction between [Cp\*Rh(H<sub>2</sub>O)<sub>3</sub>]<sup>2+</sup> and three small molecules, namely p-cresol (pC), 3-methylimidazole (3MI), and toluene (T), selected as mimetic of aromatic side chains

of Tyr, Trp and Phe, respectively, by using meta-dynamics (MTD) [20] and the ab initio fragment molecular orbital (FMO) method [21]. As shown in Fig. 1, starting from the encounter complexes (EC), where the a.a. mimetic (X) interacts with [Cp\*Rh(H<sub>2</sub>O)<sub>3</sub>]<sup>2+</sup> by non-covalent interactions, the ligand exchange reactions was promoted by adopting the MTD protocol obtaining the corresponding product adduct (PA), {[Cp\*Rh(η<sup>6</sup>-X)]<sup>2+</sup> · 3H<sub>2</sub>O}, where the three water molecules surround the η<sup>6</sup>-complex.

The conjugation reactions were analyzed by using the FMO method which allows splitting the system in fragments and then computing the total energy as function of the pair interaction energies (PIEs) [22]. Moreover, the energy decomposition analysis (EDA) [23, 24] of each PIE provides important information on the nature of the interactions between fragments, such as X and [Cp\*Rh]<sup>2+</sup> scaffold. Thus, MTD/FMO method allowed to characterize and monitor the evolution of conjugation reaction giving a new insight on this high chemoselective process and results has been used to suggest potential applications of Rh(III) metal drugs containing the [Cp\*Rh]<sup>2+</sup> scaffold.

## Methods

The structures of EC1, EC2, and EC3, retrieved from the previous study [19], were optimized at the B3LYP level of theory by using the all-electron 6-311+G(d,p) basis set for all non-metal atoms. The Rh atom was treated with the LANL2DZ basis set which includes the LANL2 pseudopotential to describe the core electrons and a Hay and Wadt double-zeta basis set to describe the valence shell electrons. Vibrational frequency calculations were then performed at the same level of theory to estimate the zero point energy (ZPE), the thermal corrections, and the gas phase vibrational entropies. The same scheme was employed to optimize the structures of the corresponding η<sup>6</sup>-complexes. The effect of explicit water on the stability of these complexes was also evaluated by including one, two and three water molecules obtaining the corresponding hydrated complexes which were optimized at same level of theory. Then, the single point energy of all the optimized geometries was calculated with ωB97X-D functional (same basis set employed in the geometry optimization) and simulating the water effect with CPCM method. Indeed, the ωB97X-D hybrid functional has been demonstrated to reproduce with good accuracy the energy of several metal complexes [25–27], and therefore, it was here employed to assess the relative stability of conjugated complexes. The free energies (G) and enthalpies (H) computed at B3LYP/CPCM/ωB97X-D level of theory were obtained as follows:

$$G = E_{\text{sol}} + G_{\text{therm}} \quad (1)$$

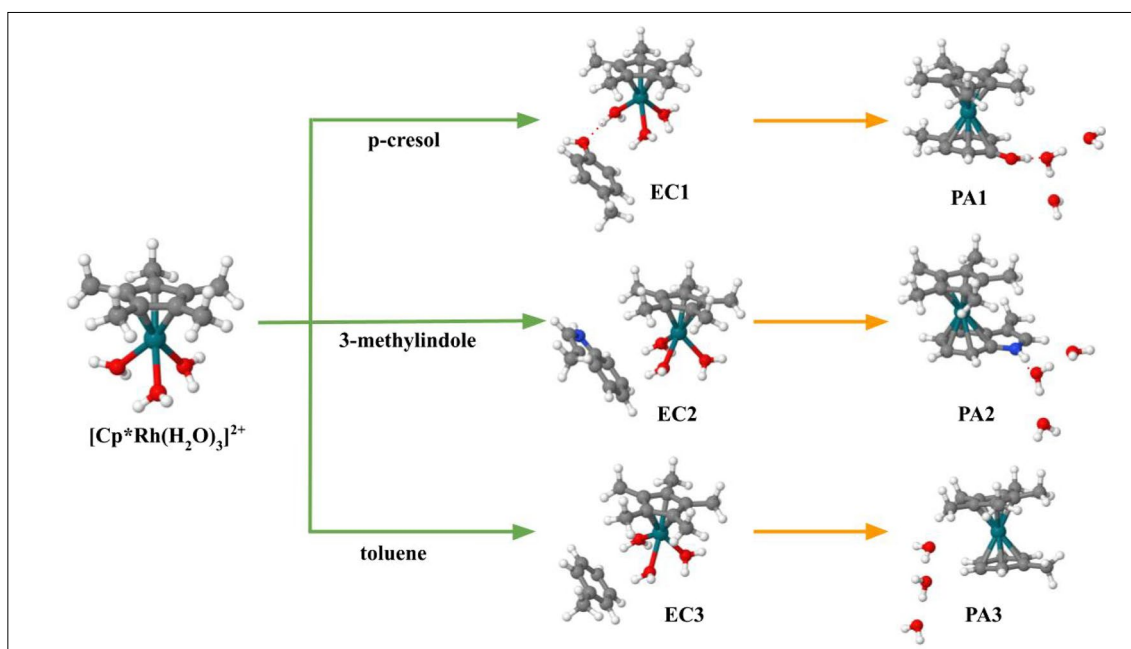


**Fig. 1** Schematic representation of ligand exchange reaction involving  $[\text{Cp}^*\text{Rh}(\text{H}_2\text{O})_3]^{2+}$  and three small molecules selected as mimetic of aromatic a.a. side chain as p-cresol (**pC**), 3-methylindole (**3MI**),

and toluene (**T**). The conjugation reactions, that starting from encounter complexes (ECs) lead to product adducts (PAs), are reported by using orange arrows

$$H = E_{\text{sol}} + H_{\text{therm}} \quad (2)$$

where  $E_{\text{sol}}$  is the electronic energy calculated at CPCM/ $\omega$ B97X-D level of theory, and  $H_{\text{therm}}$  and  $G_{\text{therm}}$  are the sum of several correction terms: zero-point energy, enthalpy, and entropy corrections (included only in  $G_{\text{therm}}$ ), computed at B3LYP level of theory in gas phase.

All DFT calculations were performed with Gaussian 09 package [28].

Meta-dynamics RMSD (MTD(RMSD)) [29] calculations at GFN2-xTB level of theory [30], implemented in xTB software [31], were performed to model the EC  $\rightarrow$  PA process (vide infra). The standard root-mean-square deviation (RMSD) in Cartesian space was used to define the collective variables (CVs). Here, the oxygen atoms of the three water molecules were considered to initialize the RMSD criteria, and define the CVs that pushed these three water molecules away from the Rh atom during the simulations — and allowed the coordination of the aromatic fragment on the metal center. The scaling factor for RMSD criteria ( $k_{\text{push}}$ ) was set to 0.05 with a width of the Gaussian potential (alpha) used in the RMSD criteria of 0.9.

All systems were simulated for 100 ps using the GBSA implicit solvent model, in NVT conditions at 298.15 K, with an integration step 2.0 fs. Each MTD trajectory was composed by sampling one snapshot per 50.0 fs, and a final representative subset of 100 structures for each

run was finally gained with a sampling rate of 1 ps. The MTD(RMSD) simulation was performed in two replicates (two runs) for each EC.

In order to assess the stability of each EC, we also performed 50 ps MD calculations for each of them, by essentially adopting the same set-up scheme but without applying the MTD(RMSD) protocol.

To avoid that non covalent binding molecules move away during MTD and MD simulations, all the EC structures were confined by a repulsive spherical potential (potential = logfermi; sphere: auto, all).

The representative structures of MTD(RMSD) and MD trajectories were then minimized at GFN2-xTB level of theory, using the GBSA model to simulate the solvation effect.

The optimized geometries resulting from either MTD or MD studies were then analyzed by using the fragment molecular orbitals (FMO) methodology and adopting the three-body approach (FMO3) [32]. Notably, although the FMO method is widely applied for the investigation of interactions involving large biological systems as proteins structure [33, 34], protein–protein interaction [35, 36], protein–DNA interaction [37] and ligand–receptor complexes [38, 39], it can be used also to study small metal complexes as previously done [40]. Here, the FMO method can be profitably used to monitor the ligand exchange reactions in terms of pair interaction energies (PIEs) because the composition of the fragments is not altered by the breaking/formation of coordinate bonds during reaction.

All FMO calculations were performed at RI-MP2/6-311G level of theory [41] adopting the triple- $\zeta$  model core potential (MCP-TZP) for the Rh atom [42]. The water solvation effect was simulated through the PCM[1] method, by computing the repulsion and dispersion contributions by the empirical method of Floris and Tomasi [43], using a high density of tesserae on the cavity surface (NTSALL = 240) and FIXPVA as tessellation scheme [44]. The solvent screening effect was simulated using the partial screening method (MODPAR=73) [45]. To prevent overestimation of charge transfer energy [46, 47], the screened point charges were adopted and the ESP-PTC was computed using the charge damping [48] for all atoms with  $a=b=1$  (SCREEN=1,1; RESPPC = -1).

The structures were split in five fragments as shown in Fig. 2:  $[\text{Cp}^*\text{Rh}]^{2+}$  (fragment 1), three distinct fragments each one including one water molecule (fragments 2, 3, and 4) and X (fragment 5).

The FMO calculations also included the energy decomposition analyses (EDA) with FMO3 corrections [49] in which each PIE value is decomposed as follows:

$$\text{PIE}_{ij} = E^{\text{es}} + E^{\text{ex}} + E^{\text{ct}} + E^{\text{disp}} + E_{\text{solv}} \quad (3)$$

where the terms  $E^{\text{es}}$ ,  $E^{\text{ex}}$ ,  $E^{\text{ct}}$ ,  $E^{\text{disp}}$ , and  $E_{\text{solv}}$  refer to electrostatic, exchange repulsion, charge transfer, dispersion and solvation energies, respectively. These terms provide important information on the nature of the interfragment interactions and disclose the energy components playing the main role in the binding process. The  $E^{\text{es}}$  component is related to Coulomb interaction between charged or polarized fragments. The  $E^{\text{ex}}$  term is always repulsive and can be ascribed to steric repulsion between close fragments. The

$E^{\text{ct}}$  component is related to the interaction between occupied orbitals of a donor and unoccupied orbitals of an acceptor. The dispersion energy term,  $E^{\text{disp}}$ , takes into account the contribution of the interaction between the temporary dipole moments of two fragments, especially important for residues not exposed to the solvent and involved in the hydrophobic interactions [50].

In analogy with ligand-receptor study [46], an estimation of the stability of the ECs is provided by the sum of PIEs between X and all fragments of  $[\text{Cp}^*\text{Rh}(\text{H}_2\text{O})_3]^{2+}$  (fragments 1, 2, 3, and 4):

$$E^{\text{INT}} = \sum_{i=1}^4 \text{PIE}_{Xi} \quad (4)$$

For each EC and PA structure, we also computed the total PIE (TPIE), i.e., the sum of all PIEs within the structure:

$$\text{TPIE} = \sum_{i>j}^N \text{PIE}_{ij} \quad (5)$$

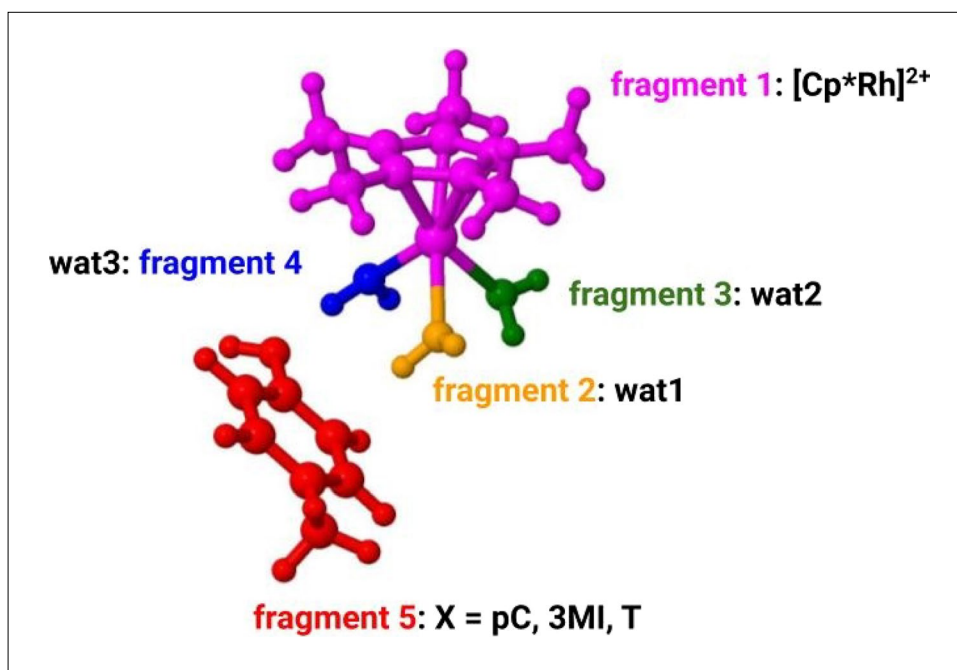
All FMO calculations were performed by using the GAMESS-US package (version: 30 June 2021 — R1) [51].

## Results

### Thermodynamics of PAs formation

The thermodynamics of EC  $\rightarrow$  PA processes was preliminary assessed at DFT level of theory (see above). All the possible configurations of the three water molecules in each of the **PA1-3** complexes were manually built and

**Fig. 2** Fragmentation scheme employed in FMO calculations where X is **pC**, **3MI**, and **T**.  $[\text{Cp}^*\text{Rh}]^{2+}$ ,  $\text{H}_2\text{O}$  (wat1),  $\text{H}_2\text{O}$  (wat2),  $\text{H}_2\text{O}$  (wat3), and X were included in fragments 1 (magenta), 2 (orange), 3 (green), 4 (blue), and 5 (red), respectively





minimized. The most stable structures were then used to calculate the free energy and enthalpy values for the EC → PA reaction (Fig. 1 and S1).

All examined processes were characterized by negative  $\Delta G$  (Table 1) suggesting that the ligand exchange reaction, EC → PA, is thermodynamically favorable for each of the X ligands. The most negative value was computed for the PA1 formation with the following order  $\Delta G1 < \Delta G2 < \Delta G3$  indicating that the pC is able to replace the three water molecules with more efficiency than 3MI and T. This result is in good agreement with our previous study where we estimated the same trend, pC > 3MI > T, for the formation of  $\eta^6\text{-[Cp}^*\text{Rh(X)]}^{2+}$  complex [19].

With exception of reaction EC2 → PA2, the reaction  $\Delta G$  values are appreciably close to the corresponding  $\Delta H$  values, presumably because of the small vibrational entropy variation accompanying this substitution process. Thus, the exergonicity of the EC → PA process estimated by our approach is mostly determined by the reaction enthalpy that quantifies the energy gain for the replacement of O → Rh with  $\pi$  → Rh bonds and for the formation of hydrogen bonds between the released water molecules.

In the framework of application of the FMO method, the  $E^{\text{INT}}$  has been used as an estimation of reaction  $\Delta H$ , for example in receptor-ligand binding processes [52]. The  $\Delta H$  of a reaction,  $\Delta_r H$ , can be also computed as difference

**Table 1**  $\Delta G$ ,  $\Delta H$ , and relative  $\Delta H$  ( $\Delta H_{\text{rel}}$ ) of the three ligand exchange reaction, EC1 → PA1, EC2 → PA2, EC3 → PA3 investigated in this work, computed at B3LYP/6-311+G(d,p)// $\omega$ B97X-D/6-311+G(d,p). The total pair interaction energies ( $\Delta\text{TPIE}$ ) are reported along with the corresponding relative values. All energy values are in kcal/mol

Reaction	$\Delta G$	$\Delta H$	$\Delta H_{\text{rel}}$	$\Delta\text{TPIE}$	$\Delta\text{TPIE}_{\text{rel}}$
EC1 → PA1	-14.9	-14.6	0.0	-25.1	0.0
EC2 → PA2	-12.7	-9.7	4.9	-19.5	5.6
EC3 → PA3	-7.6	-7.8	6.8	-17.4	7.6

between the sum of enthalpy variation of formed bonds and the sum of  $\Delta H$  of the broken bonds. Thus, considering that in EC → PA reaction there are only ligands exchange without breaking of pure covalent bonds, the  $\Delta H$  of such reaction can be estimated in principle by considering the difference between PIE values of the broken and formed ligands interactions passing from EC to PA ( $\Delta\text{TPIE}$ ):

$$\begin{aligned} \Delta_r H &= \left[ \sum \Delta H(\text{formed bonds}) - \sum \Delta H(\text{broken bonds}) \right] \\ &\approx \Delta\text{TPIE} = \text{TPIE}_{\text{PA}} - \text{TPIE}_{\text{EC}} \end{aligned} \quad (6)$$

where  $\text{TPIE}_{\text{PA}}$  and  $\text{TPIE}_{\text{EC}}$  are the total pair interaction energies computed according Eq. (5) for PA and EC, respectively.

As reported in Table 1,  $\Delta\text{TPIE}$  terms reproduce quite well the trend of  $\Delta H$  values (they are all 10 kcal/mol higher in energy), especially the relative values with an error < 1 kcal/mol, suggesting that the FMO method might be used to estimate the  $\Delta H$  of EC → PA reaction and compare the ligand exchange efficiencies of pC, 3MI, and T.

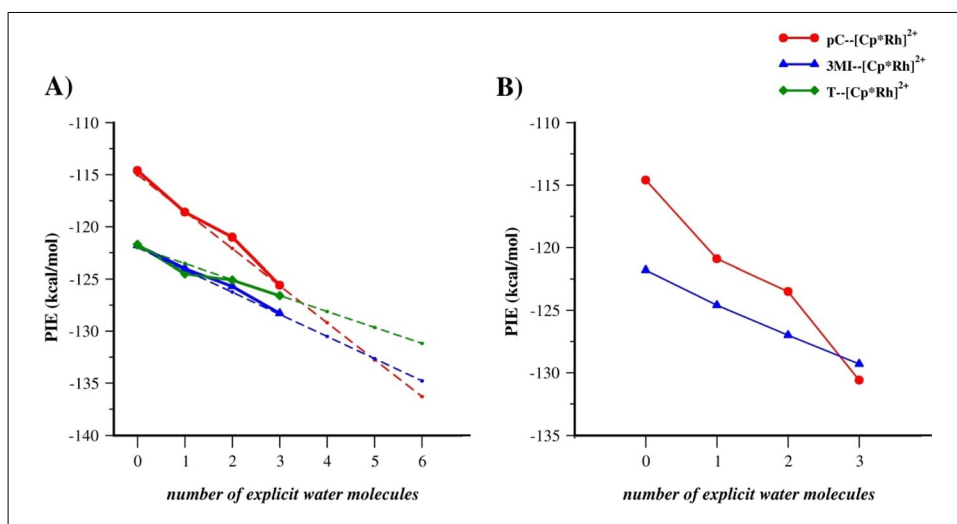
### MTD/FMO descriptions of PAs formation

To explore the EC → PA reaction path, we simulated each encounter complex (two production runs of 100 ps per EC) using the MTD(RMSD) protocol implemented in xTB. The pushing potential was applied only to the oxygen atoms of the coordinated water molecules. Being the system simulated into a spherical confinement and implicit solvation, the gradually decomplexed water molecules last in proximity of the system, thus, potentially influencing the approach and coordination of the X ligand at the metal fragment. To assay the impact of non-coordinated water molecules on the stability of the system, the geometry of the  $[\text{Cp}^*\text{Rh(X)}]^{2+}$ ,  $\{[\text{Cp}^*\text{Rh(X)}]^{2+} \cdot \text{H}_2\text{O}\}$ ,  $\{[\text{Cp}^*\text{Rh(X)}]^{2+} \cdot (\text{H}_2\text{O})_2\}$ , and  $\{[\text{Cp}^*\text{Rh(X)}]^{2+} \cdot (\text{H}_2\text{O})_3\}$  were optimized at DFT level of theory by testing several configurations of explicit water molecules. Then, the most stable structures (Fig. S1) were analyzed with the FMO3 scheme [1].

As shown in Fig. 3A and Table S1, the X--[Cp\*Rh]<sup>2+</sup> PIEs without including explicit water molecules are almost the same for 3MI and T (−121.8 and −121.7 kcal/mol, respectively) while a less negative value was found for pC (−114.6 kcal/mol). Including one, two, and three explicit water molecules the X--[Cp\*Rh]<sup>2+</sup> PIE decreases (more negative values). The curves related to pC--[Cp\*Rh]<sup>2+</sup> and 3MI--[Cp\*Rh]<sup>2+</sup> PIEs significantly decrease indicating that the interactions with explicit waters affect mainly the two scaffolds able to establish H bonds with water which increase the electron density on the aromatic rings. Notably, the pC--[Cp\*Rh]<sup>2+</sup> PIE is characterized by the steepest curve although the X--[Cp\*Rh]<sup>2+</sup> PIE still follows the trend 3MI > T > pC. Interestingly, by assuming an almost linear trend of PIE decrease and the cooperative effect of H bonds, we estimated that T > 3MI > pC trend of X--[Cp\*Rh]<sup>2+</sup> PIE is gained with six explicit water molecules (Fig. 3A). Because the accuracy of FMO calculations increases by increasing the size (number of atoms) of fragments, a second set of FMO calculations were performed on the systems with X=3MI and pC by including the H-bond interacting water molecule to the latter fragments and evaluating the corresponding X--[Cp\*Rh]<sup>2+</sup> PIE values (Fig. 3B, Table S1).

Although the PIE of pC--[Cp\*Rh]<sup>2+</sup> was found to be larger compared to 3MI--[Cp\*Rh]<sup>2+</sup> in the system with

**Fig. 3** PIE values of pair formed by X and  $[\text{Cp}^*\text{Rh}]^{2+}$  scaffold by varying the number of explicit waters (from zero to three) **A**) including X,  $[\text{Cp}^*\text{Rh}]^{2+}$ , and water molecules in separated fragments and **B**) including X and water directly interacting via H bond in the same fragment. In Fig. 3A, the trend lines are also reported



no explicit water, the former decreases more steeply and becomes lower than the  $3\text{MI}-[\text{Cp}^*\text{Rh}]^{2+}$  PIE when three water molecules were considered ( $-130.6$  and  $-129.3$  kcal/mol, respectively). Thus, to correctly reproduce the interaction strength of the three aromatic mimetics of a.a. side chains by using the FMO3 method the inclusion of at least three explicit water molecules are needed and that one directly involved in H bond with aromatic scaffold should be included in its same fragment.

The PIE values of all the fragments coordinated to the  $[\text{Cp}^*\text{Rh}]^{2+}$  scaffold, namely  $\text{X}-[\text{Cp}^*\text{Rh}]^{2+}$ ,  $\text{wat1}-[\text{Cp}^*\text{Rh}]^{2+}$ ,  $\text{wat2}-[\text{Cp}^*\text{Rh}]^{2+}$ ,  $\text{wat3}-[\text{Cp}^*\text{Rh}]^{2+}$ , for each X ligand, and retrieved from the corresponding MTD trajectories are reported in Fig. 4.

For X = **pC** (Fig. 4A and B), the aromatic ligand displaced the first water molecules (wat3, blue line) in a few ps. In the first MTD run (Fig. 4A), the second water molecules (wat1, orange profile) was replaced at 10 ps with consequent increasing of  $\text{pC}-[\text{Cp}^*\text{Rh}]^{2+}$  interaction (more negative value of PIE). A similar trend of substitution of the first and second water was observed also in the second run (Fig. 4B). The last water molecule is released around 50 ps of the first run with formation of the  $\eta^6$ -complex, which remains stable until the end of simulation (100 ps). Notably, in this segment of trajectory the PIE of  $\text{X}-[\text{Cp}^*\text{Rh}]^{2+}$  assumes an average value of  $-122.0 \pm 1.6$  kcal/mol (Table S2) while the PIE between water molecules and  $[\text{Cp}^*\text{Rh}]^{2+}$  are close to zero indicating that they are not bound to the metal scaffold. Whereas in second run (Fig. 4B), the  $\eta^6$ -complex is formed before 50 ps although, at about 60 ps, one water molecule (wat1) came back to coordinate at  $[\text{Cp}^*\text{Rh}]^{2+}$  breaking the  $\eta^6$  coordination of **pC** for 20 ps before its restoration at the end of trajectory.

The formation of  $[\text{Cp}^*\text{Rh}(\eta^6\text{-X})]^{2+}$  complex was also detected before 50 ps in both runs of **3MI** and **T**,

but these complexes lasted for a shorter time compared to **pC** (Fig. 4C–F). The average  $3\text{MI}-[\text{Cp}^*\text{Rh}]^{2+}$  and  $\text{T}-[\text{Cp}^*\text{Rh}]^{2+}$  PIE in the  $\eta^6$  coordination were  $-130.4 \pm 11.8$  and is  $-128.8 \pm 1.1$  kcal/mol; hence, slightly more negative compared to  $\text{pC}-[\text{Cp}^*\text{Rh}]^{2+}$  PIE (Table S2).

The energy decomposition analyses (EDA) of the  $\text{X}-[\text{Cp}^*\text{Rh}]^{2+}$  PIE calculated in the MTD(RMSD) simulations were also performed. As shown in Fig. S2,  $E^{\text{es}}$  and  $E^{\text{ct}}$  are the terms that mostly contribute to determining negative PIE values.  $E^{\text{sol}}$  and  $E^{\text{ex}}$  are always positive terms and reach the highest values in  $\eta^6$  coordination due to the steric clashes between methyl groups of  $\text{Cp}^*$  and aromatic scaffold.

We also computed the average values of the EDA terms for all examined  $\eta^6$ -complexes in the MTD trajectories, and the results are reported on Table S2. Notably, the average  $E^{\text{ct}}$  values followed the **pC** < **3MI** < **T** trend, and the most negative value for **pC** ( $-130.9$  kcal/mol) compared with **3MI** and **T** ( $-127.7$  and  $-128.3$  kcal/mol, respectively). Therefore, we observed that the trend of CT from X to  $[\text{Cp}^*\text{Rh}]^{2+}$  over all the trajectory is complementary to the FMO3 charge of  $[\text{Cp}^*\text{Rh}]^{2+}$  fragment,  $Q_3$ , whose decrease from +2 to  $\sim +1.5$  is mainly due to the CT from X (Fig. S3–S4).

The hapticity ( $\eta$ ) variation of the X scaffold during the reaction path was evaluated by computing the distance between Rh and C atoms of aromatic scaffold (**pC**, **3MI**, and **T**) along all the trajectories (Fig. 5). In the case of **pC** and **3MI**, the O-Rh and N-Rh distances, respectively, were also monitored.

This analysis provides an interesting result for **pC** ligand. Indeed, the metal coordination of OH anticipates the replacement of the first water molecule by means of C atoms of benzene scaffold at the beginning of the trajectory of run1 (Figs. 5A and 6A). Then, around 9 ps,  $\text{C}_1$  and  $\text{C}_2$  of the benzene ring (Figs. 6A, 9 ps) start to

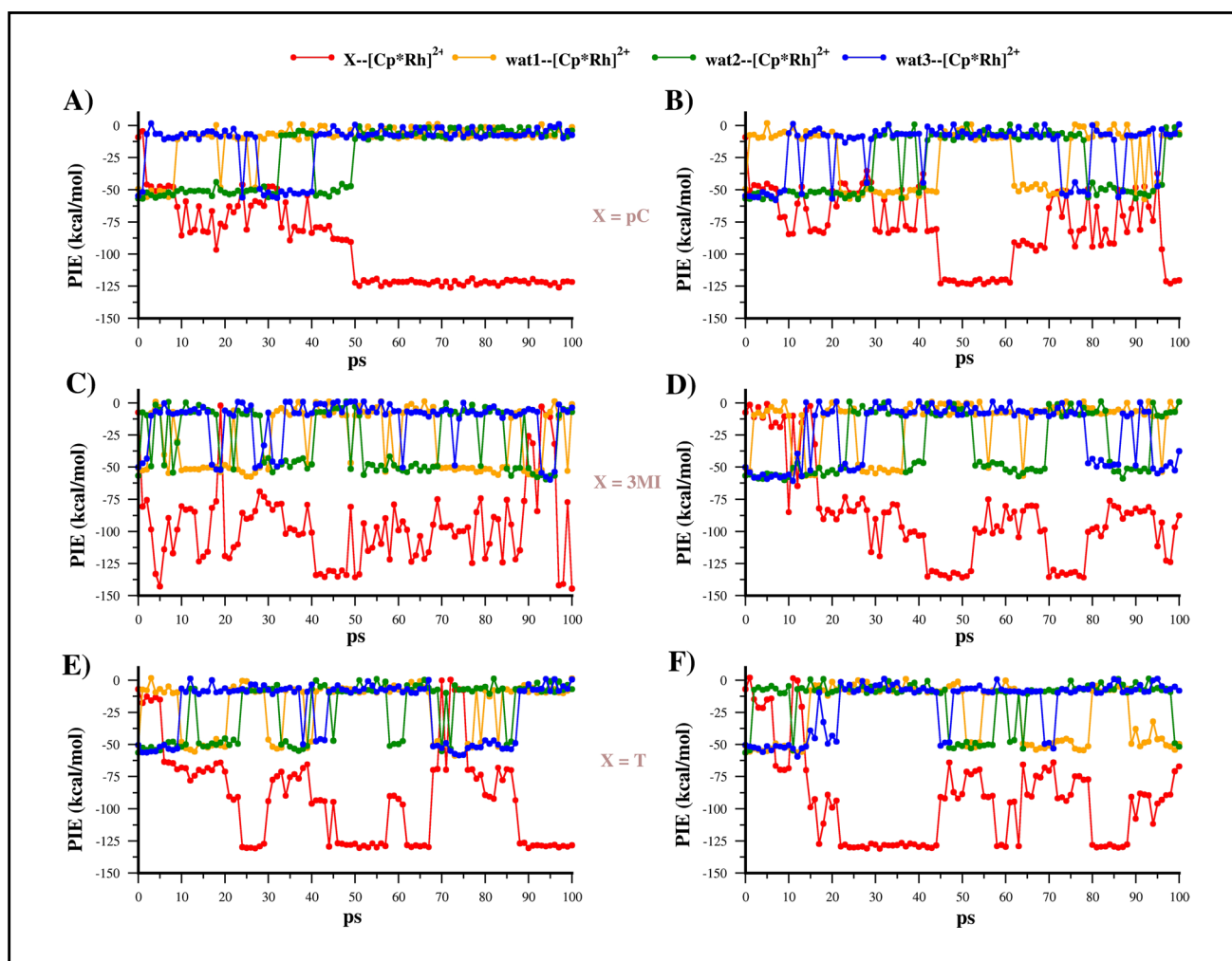


**Fig. 4** PIE values of fragments interacting with  $[\text{Cp}^*\text{Rh}]^{2+}$  computed for the sampled structures of MTD(RMSD) run1 and run2 of **EC1** (A and B), **EC2** (C and D), and **EC3** (E and F)

coordinate the Rh ion leading to a peculiar  $\eta^3$ -complex with the  $\text{OC}_1\text{C}_2$  coordination of the phenol moiety. This configuration remains stable for ca 30 ps before the O-Rh interaction is replaced by other aromatic C atoms leading to the transient  $\eta^4$  intermediate that rapidly evolves in the  $\eta^6$ -complex. This trend was also observed in run2 (Fig. 5B), where the simultaneous coordination of Rh by means of OH and two aromatic C atoms is observed also in the 70–95 ps segment of the trajectory. Thus, these results indicate that the OH group plays a crucial role, especially in the early stages of the interaction between **pC** and  $[\text{Cp}^*\text{Rh}(\text{H}_2\text{O})_3]^{2+}$  complex.

The analysis of C-Rh distances of reaction involving the **EC2** indicates that, in first run, the first leaving water molecule is replaced by atom  $\text{C}_4$  and  $\text{C}_5$  of the indole leading to the  $\eta^2$ -complex (Figs. 5C and 6B). In about 37 ps, the hapticity of the phenyl ring becomes transiently  $\eta^4$  and then  $\eta^6$  in a few ps. Interestingly, at around 55 ps, the  $[\text{Cp}^*\text{Rh}]^{2+}$

moiety starts interacting with the  $\text{C}_2$  and  $\text{C}_3$  of the pyrrolic portion of **3MI**, reaching the  $\eta^5$  at 60 ps (Fig. 6B). Then, the  $[\text{Cp}^*\text{Rh}]^{2+}$  scaffold moves from pyrrolic to phenyl ring during in the later stages of the trajectory. Conversely, in the second run (Fig. 5D), we observed the involvement the phenyl ring only in the Rh-coordination of **3MI**. Notably, in both runs, the  $\eta^4$  coordination of **3MI** is maintained only for a few steps in the transit between  $\eta^2$  and  $\eta^6$  coordination.

The same scenario was found also for **T** complexes where the most recurring coordination motives are  $\eta^2$  and  $\eta^6$  while  $\eta^4$  is only transiently detected. The analysis of C-Rh distance reveals that, in spite of the early detachment of the first water molecule, the  $\eta^2$  coordination of **T** at Rh is not concomitant, as shown in Figs. 5E and F and 6C. Indeed, in the early 10 ps of the first run, **T** interacts with Rh only via weak electrostatic interaction of  $\pi$ -electrons of  $\text{C}_1\text{-C}_2$  bond which rapidly evolves in  $\eta^2$  coordination by means of  $\text{C}_3$  and  $\text{C}_4$  (Fig. 6C). This

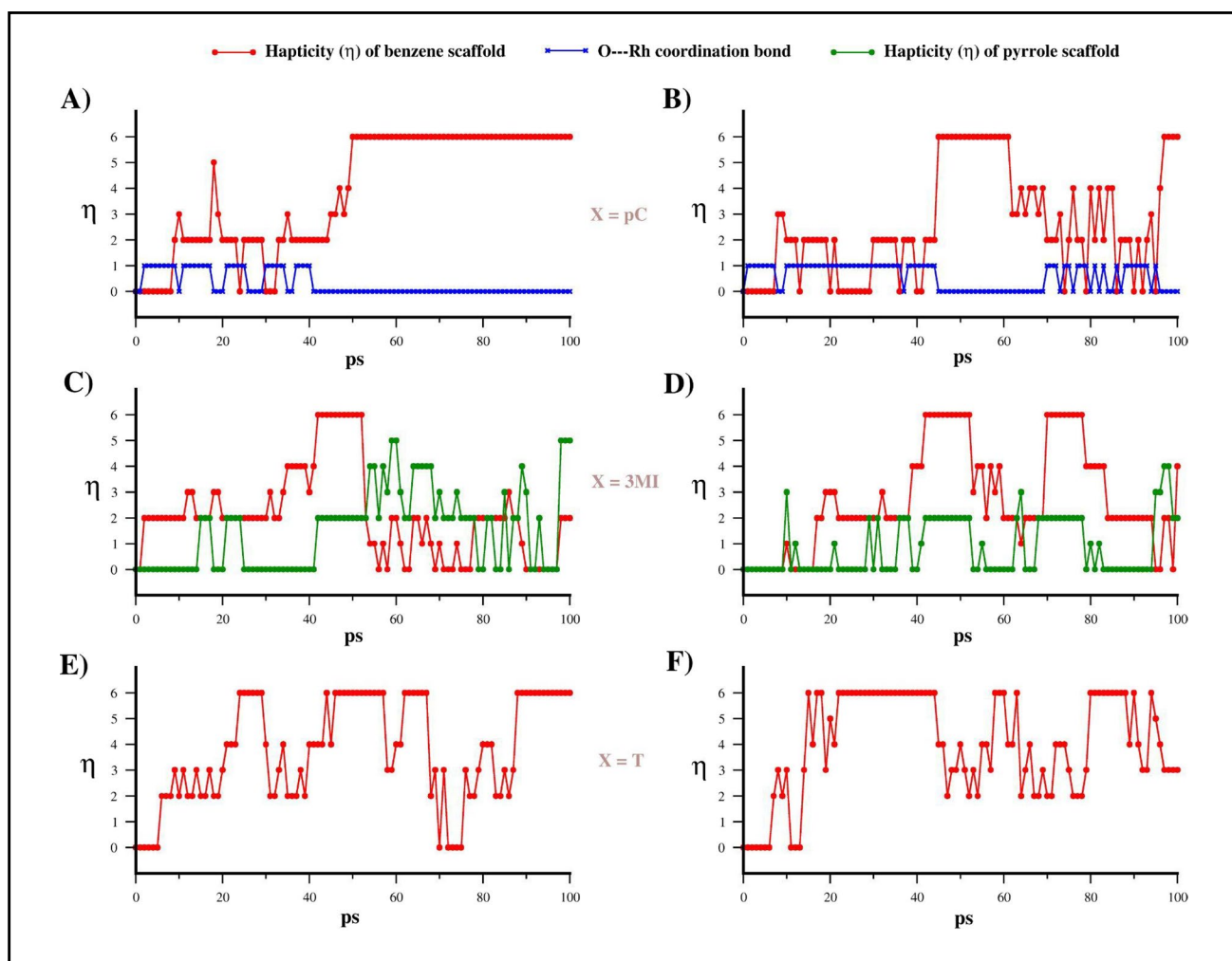


**Fig. 5** Estimation of hapticity of  $X\text{-}[\text{Cp}^*\text{Rh}]^{2+}$  interaction computed on the base of C-Rh distance for structures of MTD(RMSD) run 1 and 2 for **EC1** (A and B), **EC2** (C and D), and **EC3** (E and F). For **EC1** (A and B) and **EC2** (C and D), the presence of a chemical bond between phenolic O and pyrrolic N atoms with Rh are reported by

using blue and green lines, respectively. We assumed a C-Rh or N-Rh bond formed when the distance between C/N and Rh is below to 3 Å while the OH (**pC**) is considered bounded to Rh when O-Rh distance is below 2.5 Å

evidence suggests a certain difficulty for **T** to initiate the interaction with Rh which should lead to the water displacement.

Notably, at 70 ps, **T** loses the contact with Rh restoring for few ps the  $[\text{Cp}^*\text{Rh}(\text{H}_2\text{O}_3)]^{2+}$  complex (Fig. 5E), although this event was observed only in run1. Indeed, in the second run, **T** interacts with Rh for the entire trajectory with continuous interchanging between  $\eta^2$  and  $\eta^6$  coordination.

### MD/FMO analysis of ECs stability

In analogy with ligand-receptor studies [26], the interaction energy between X and  $[\text{Cp}^*\text{Rh}(\text{H}_2\text{O}_3)]^{2+}$  can be estimated as the overall interfragment PIE named  $E^{\text{INT}}$  (Eq. 4).

The computed  $E^{\text{INT}}$  values for **EC1**, **EC2**, and **EC3** are  $-17.5$ ,  $-14.4$ , and  $-10.3$  kcal/mol, respectively, suggesting that **pC** might effectively form a more stable EC with  $[\text{Cp}^*\text{Rh}(\text{H}_2\text{O}_3)]^{2+}$  than **3MI** and **T** (Table S3).

Thus, considering that the formation of a stable EC is an important checkpoint of the conjugation process, we performed 50 ps MD simulations, to follow up the formation of **EC1-3** complexes in native condition, i.e., without using the MTD(RMSD) protocol. The snapshots obtained by sampling each 10 ps of the **EC1**, **EC2**, and **EC3** trajectories are reported in Fig. 7, while the corresponding FMO analysis was summarized in Figs. 8 and S6.

The **pC** ligand establishes H bond interactions with one or two water molecules by means of OH group (Fig. 7A), during the most part of trajectory, and with an average  $E^{\text{INT}}$



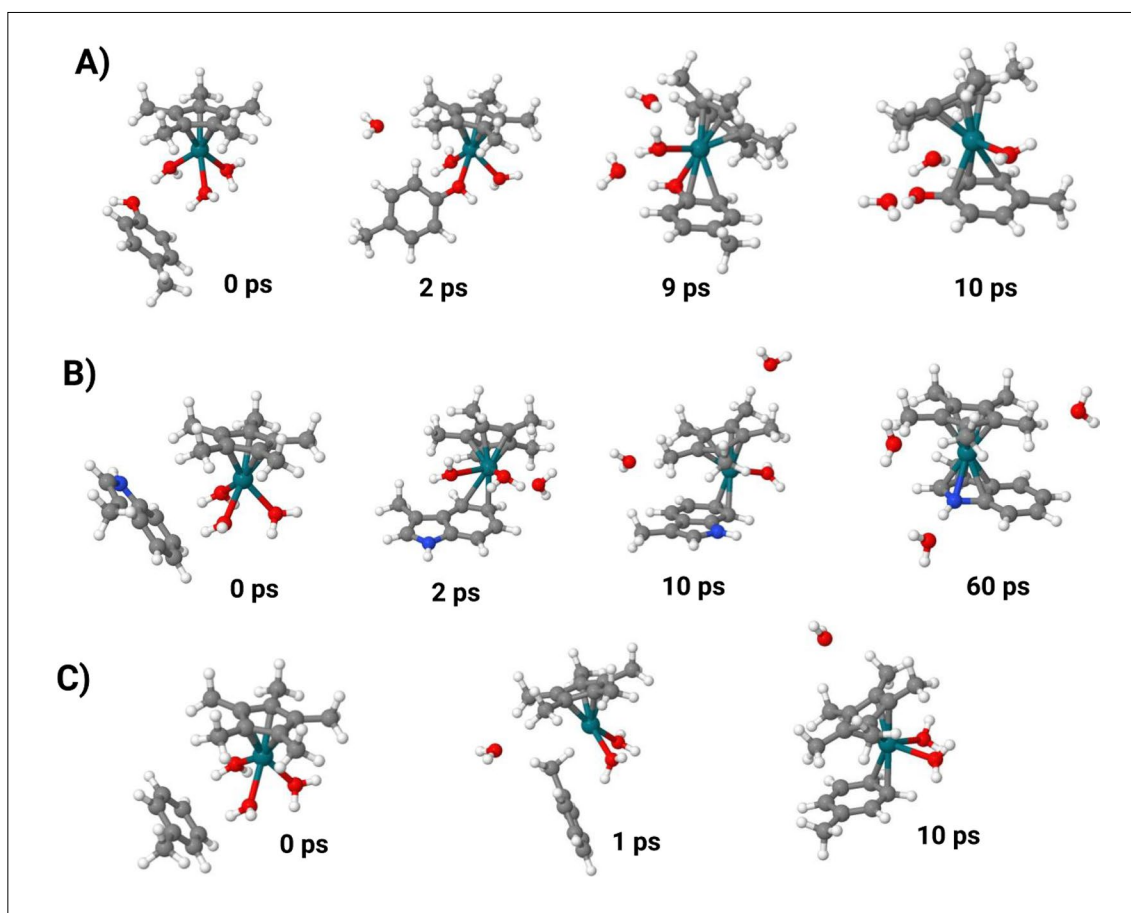


**Fig. 6** Most relevant structures of the first 10 ps of MTD(RMSD) run1 for **A) EC1**, **B) EC2**, and **C) EC3**

value of  $-12.5$  kcal/mol (Fig. 8A). Moreover, we detected that, in the early stages of the simulation (13–14 ps), the OH group established a coordinate bond with Rh by forming the adduct  $[\text{Cp}^*\text{Rh}(\text{H}_2\text{O})_3(\text{pC})]^{2+}$ , in which the three water molecules and the OH function of **pC** coordinated the  $[\text{Cp}^*\text{Rh}]^{2+}$  metal center (Fig. S6). In this structure, the X- $[\text{Cp}^*\text{Rh}]^{2+}$  PIE reaches the most negative values of the trajectory ( $\sim -41.5$  kcal/mol) while the X-wat1 interaction energy is positive due to the lacking of any H bond with the OH function, and to the occurrence of steric clashes (Fig. 8B).

Therefore, the analysis of the PIE values between water molecules and  $[\text{Cp}^*\text{Rh}]^{2+}$  in the latter complex showed an important decrease of these interfragment energies, compared with values computed at 12 ps, suggesting a weakening of the Rh-water interaction. This data was corroborated by the increased wat-Rh bond lengths (Fig. S6), with highest value of  $0.25$  Å computed for wat3-Rh interaction. It is worth noting that wat3, found to be majorly affected by the O-coordination of the phenol moiety, was also detected as the first molecule replaced by OH in the MTD run1, thus we speculate that the **EC1** structures sampled at 13 and 14 ps of the MD run may recall the transition state structure for the

release of the first water molecule. All these results indicate that the OH function of the phenol ligand is able to exert a strong influence on the stability of the first coordination sphere of the Rh(III) center, and it could attack the metal center in native conditions, i.e., even in absence of a pushing potential on the water oxygen.

On the contrary, for both **3MI** and **T** the weak interaction between the  $\pi$ -electrons of aromatic rings and H atoms of Rh-bound waters, characterizing the starting **EC2** and **EC3** structures, are rapidly break within the first ps of simulations and replaced by  $\pi$ - $\pi$  interactions between  $\text{Cp}^*$  ring and the aromatic scaffold of ligands (Fig. 7B and C) assuming a “reversed sandwich-like” configuration. The analysis of their  $E^{\text{INT}}$  and of the corresponding PIEs reflects these structural rearrangements of **EC2** and **EC3** (Fig. 8C–D and E–F, respectively). This binding mode, favored by hydrophobic and dispersion interactions, is stable over the most part of trajectories for both **3MI** and **T** with average  $E^{\text{INT}}$  of  $-12.5$  and  $-6.2$  kcal/mol, respectively (Fig. 8C and E). Notably, in this configuration, the ligand exchange reaction leading to PA cannot occur since the aromatic scaffold cannot attack the metal center.

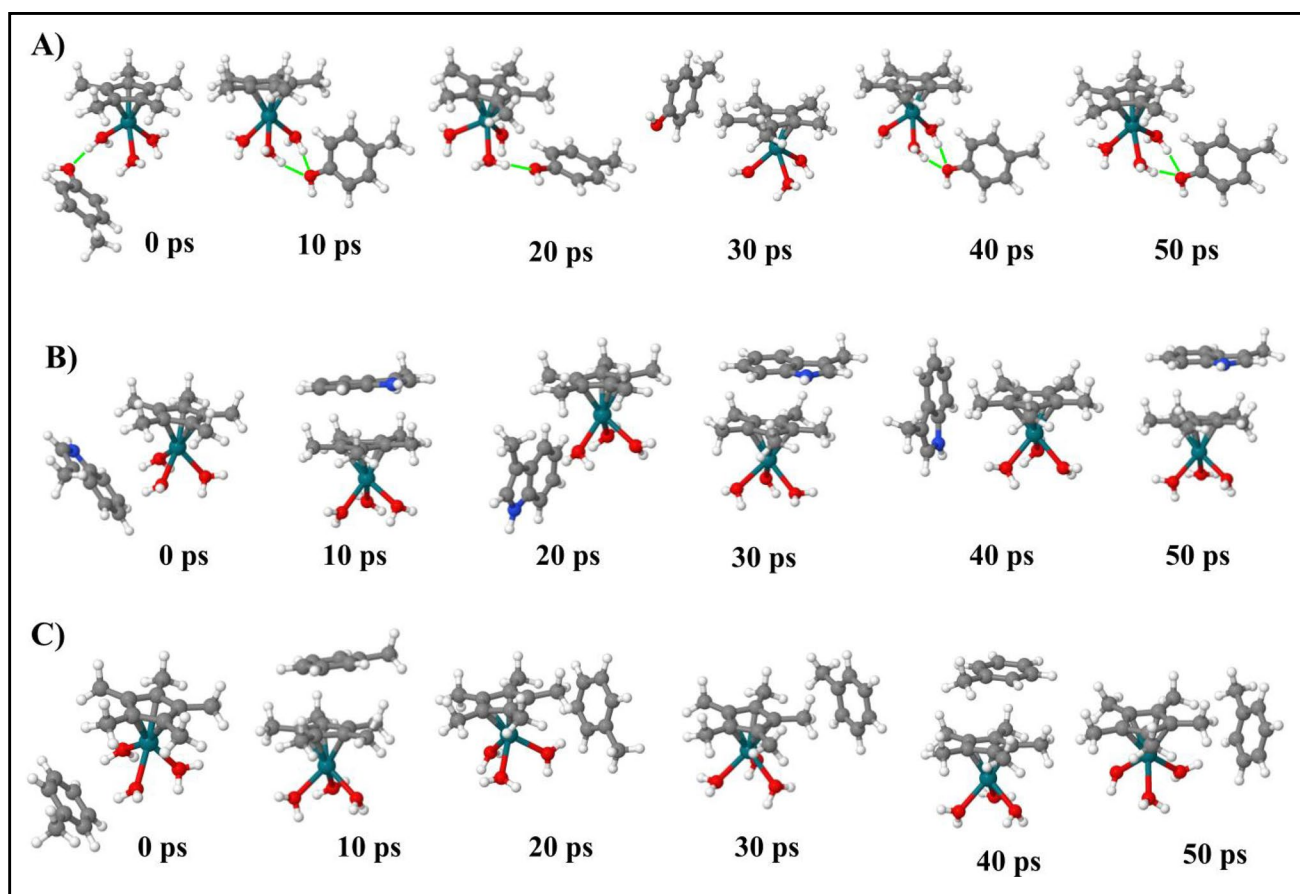


**Fig. 7** Representative structures of MD trajectories obtained without applying the MTD(RMSD) protocol starting from **A) EC1**, **B) EC2**, and **C) EC3** collected at 0, 10, 20, 30, 40, and 50 ps

## Discussion

The cationic  $[\text{Cp}^*\text{Rh}(\text{H}_2\text{O})_3]^{2+}$  complex can react in water, and in mild pH conditions, with an aromatic scaffold, **X**, leading to the exchange product,  $[\text{Cp}^*\text{Rh}(\eta^6\text{-X})]^{2+}$ . Designed to be employable to targeting the aromatic side chain of a.a. as Tyr, Trp, and Phe, this reaction has disclosed a high chemoselectivity for the conjugation of the Tyr phenol compared to the Trp and Phe side chains of GPCR peptides, as shown by the experimental and theoretical studies [17–19]. Indeed, many drugs acting on opioid receptors contain an aromatic ring; thus, their conjugation with  $[\text{Cp}^*\text{Rh}]^{2+}$  might be explored as a possible strategy to modulate their pharmacological and pharmacokinetic profiles. Notably, the  $[(\eta^6\text{-Cp}^*\text{Rh-Tyr}^1)\text{-Leu-enkephalin}]^{2+}$  showed an enhanced activity on the mu receptor compared with free peptide supporting the reliability of this strategy [53]. Although our previous studies [19] have provided evidences that the formation of  $[\text{Cp}^*\text{Rh}(\eta^6\text{-Tyr})]^{2+}$  complexes is thermodynamically more favorable compared to either Trp and Phe, a deeper analysis of the structural aspects underlining such a chemoselectivity is lacking. In

this work, to better characterize the main structural aspects involved in this specific ligand exchange process, we studied the reactivity of the aromatic scaffold **pC**, **3MI**, and **T**, mimetics of the aromatic side chain of Tyr, Trp, and Phe, respectively, by using DFT approaches, FMO analyses, and molecular dynamics simulations at tight-binding DFT level of theory.

The DFT investigation was focused on the conversion of the non-covalent adducts of  $[\text{Cp}^*\text{Rh}(\text{H}_2\text{O})_3]^{2+}$  with each of the a.a. mimetic scaffolds **pC**, **3MI**, and **T**, and provided the optimized structures of the encounter complexes **EC1**, **EC2**, and **EC3**, respectively, as well as those of the corresponding  $\eta^6$ -complexes plus released water molecules, **PA1**, **PA2**, and **PA3**.

These calculations essentially reproduced the previously estimated reaction free energy trend [19] characterized by the most stable product adduct formed by **pC**, **PA1** with  $\Delta G = -14.9$  kcal/mol, while **PA2** and **PA3** were less stable,  $\Delta G = -12.7$  and  $\Delta G = -7.6$  kcal/mol, respectively.

The FMO3 analysis of DFT optimized structures of **PA1-3** complexes, by taking into account the presence of three, two, one or no water molecule in the second coordination

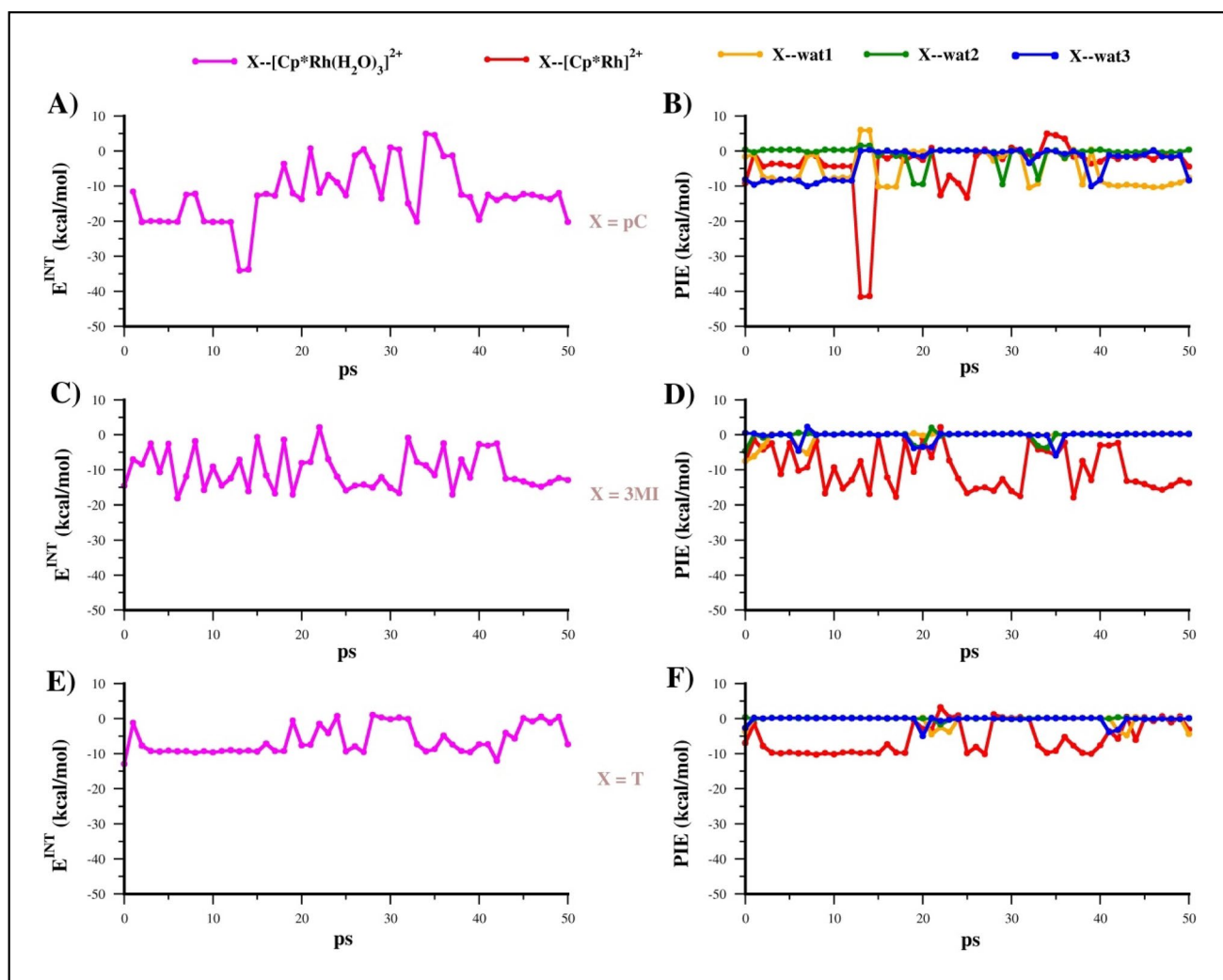


**Fig. 8**  $E^{\text{INT}}$  profiles computed for **A)** **pC**, **C)** **3MI**, and **E)** **T** along with the corresponding PIE components (figures **B**, **D**, and **F**, respectively)

sphere led us to estimate the effect of the water bulk on the interfragment interaction energy, thus, providing a direct assessment of the energy holding the stability of the  $\eta^6$ -complexes. Indeed, we found that the interfragment interactions within the  $[\text{Cp}^*\text{Rh}(\eta^6\text{-X})]^{2+}$  complexes are affected by the number of surrounding water molecules. In particular, the FMO outcomes indicated that when more than three explicit water molecules are present in the second coordination sphere, the **PA1** > **PA2** > **PA3** stability order is gained, consistently with the experimental findings [17, 18]. We envision that such an effect may be ascribed to the polarization of the OH group in the **pC** ligand, via the formation of H bonds with the bulk water molecules, that potentiates its +M effect, enhances the electronic density on benzene scaffold, and, in turn, strengthens the interaction with the  $[\text{Cp}^*\text{Rh}]^{2+}$  scaffold. Although with a less intensity, this effect was also found for **3MI**, since OH as well as NH function of **3MI**, can act as H bond donor and the interaction

with O atom of solvation water leads to rising the +M effect on aromatic scaffold.

This result suggests a possible role of solvation water also in the biological environment. Indeed, Tyr side chain can be found also in protein domains exposed to the solvent while Trp and Phe, due to their high hydrophobicity, are basically located in the buried regions. Thus, Tyr side chain should be more likely accessible from the bulk than Trp and Phe, and more exposed to the reaction with hydrophilic  $[\text{Cp}^*\text{Rh}(\text{H}_2\text{O})_3]^{2+}$  complex which is boosted by the action of solvation water molecules upon OH function increasing its +M effect and so to the **PA1** stability.

To detail the EC  $\rightarrow$  PA process at room temperature, we performed meta-dynamics simulations at the tight-binding DFT level of theory, and applied the FMO3 analysis to representative snapshots of the calculated trajectories. These calculations revealed that the chemoselective  $\eta^6$ -coordination of phenol compared to the indole and phenyl scaffolds is

ascribed to the multifacet role of the OH group. Beside its +M effect on the electron density of the aromatic group, as evidenced by the DFT studies, the MTD simulations showed its ability to initiating and assisting the release of water molecules. Indeed, the OH function in **pC**, acting as H bond acceptor, allowed this aromatic ligand to interact with one or two water molecules coordinated at the  $[\text{Cp}^*\text{Rh}]^{2+}$  scaffold. We envision that these interactions may strengthen the non-covalent interactions in **EC1**, but, concomitantly, also favor its rapid evolvement into the  $\eta^2$ -complex. In detail, we hypothesized that the OH group, once non-covalently anchored at the  $[\text{Cp}^*\text{Rh}]^{2+}$  scaffold, might directly attack the Rh center at the beginning of the ligand exchange reaction, by promoting a more effective replacement of the first water molecule than **3MI** or **T**. These latter aromatic molecules are devoid of either nucleophilic or H bond acceptor groups able to anchor at and/or attack the metallic center, and the conjugation reaction they give rise should rather start with the direct formation of the  $\eta^2$ -complex and release of one water molecule.

The MTD simulation of the **EC1** species corroborated the formation the  $[\text{Cp}^*\text{Rh}(\text{H}_2\text{O})_2(\kappa^1\text{-pC})]^{2+}$  complex, its further evolvement into the transient  $\eta^2$  and  $\eta^4$  adducts before yielding the stable  $[\text{Cp}^*\text{Rh}(\eta^6\text{-pC})]^{2+}$  complex. On the other hand, we found that  $\eta^4$  adducts are also transient complexes in the formation of **PA2** and **PA3**, even though these systems were mostly represented by the equilibrium of  $\eta^2$  and  $\eta^6$  forms. This evidence is in agreement with the DFT results indicating the lesser exergodicity in the formation of **PA2** and **PA3** compared to **PA1**.

The role of OH, and, more generally, of the non-covalent approach of the X ligand to the  $[\text{Cp}^*\text{Rh}(\text{H}_2\text{O})_3]^{2+}$  complex in the first stages of the ligand exchange reaction, was better described by the MD simulation of **EC1-3** complexes, without applying the MTD(RMSD) protocol. The Trp and Phe side chain mimetic scaffolds, **3MI** and **T**, were found to initially interact with the  $[\text{Cp}^*\text{Rh}(\text{H}_2\text{O})_3]^{2+}$  cation only by means of weak polar contacts (especially for **T**), while the phenol OH of **pC** established strong H bonds which last in the trajectory. As a consequence, the MD trajectory analysis showed the weak polar  $\pi$ -HOH contacts are rapidly broken and **EC2** and **EC3** rearrange to a sort of reversed sandwich configuration between  $\text{Cp}^*$  and aromatic rings of **3MI** or **T**, which is not favorable to the ligand exchange reaction since the aromatic scaffold cannot attack the Rh atom. As a result, the OH group not only enhanced the stabilization of the **PA1** structure compared with **PA2** and **PA3** by means of +M effect, augmented by the interaction with solvation water, but also contributed to dynamically sample a proper configuration of **EC1** where the reactive species, i.e., **pC** and  $[\text{Cp}^*\text{Rh}(\text{H}_2\text{O})_3]^{2+}$ , are correctly oriented to initiate the **EC1**  $\rightarrow$  **PA1** process. Thus, our results suggest that the OH group of phenol plays a crucial role in shaping

the high chemoselectivity in the  $\text{Cp}^*\text{Rh(III)}$ -conjugation of Tyr residues compared to Trp and Phe. Therefore, the combination of DFT studies, tight-binding DFT molecular dynamics simulations, and FMO analysis, here applied for the first time to study the ligand exchange reaction of metal complexes, provided an atomistic level of understanding of such chemoselectivity, and unveiling the importance of non-covalent interactions between **pC** and  $[\text{Cp}^*\text{Rh}(\text{H}_2\text{O})_3]^{2+}$  in both thermodynamics and kinetics of the formation of  $[\text{Cp}^*\text{Rh}(\eta^6\text{-X})]^{2+}$  X=Tyr, Trp, and Phe bioconjugates.

Our further computational work will be devoted to improve the accuracy of this computational protocol by including explicit solvation water molecules and adopting the free energy decomposition analysis based on the FMO method combined with umbrella sampling molecular dynamics (US-MD) approach, recently proposed by Fedorov et al. [54].

These mechanistic aspects can be employed in the newly development of metal drugs based on the chemoselective  $[\text{Cp}^*\text{Rh}(\text{H}_2\text{O})_3]^{2+}$  targeting of Tyr residues in endogenous peptides or proteins.

Indeed, the alterations of biological processes involving Tyr residues, such as Tyr phosphorylation [55] by means of Tyr-kinase enzymes, are found in several pathologies as in tumors [56]. Thus, the high selectivity conjugation of  $[\text{Cp}^*\text{Rh}(\text{H}_2\text{O})_3]^{2+}$  might be used to target the Tyr residues leading to  $[\text{Cp}^*\text{Rh}(\text{Tyr})]^{2+}$  and impeding the action of Tyr-kinase enzymes (Fig. 9). Moreover, the target selectivity, a crucial feature of a drug, could be facilitated by the pH of tumor microenvironments, which is often around 5.5, thus, in the optimal range of pH values for the  $[\text{Cp}^*\text{Rh}(\text{Tyr})]^{2+}$  formation. It is worth noting that Rh(III)-containing complexes were already evaluated as inhibitors of pathological process kinase-dependent acting as direct protein-kinase (PK) inhibitors via hydrogen bonds with the ATP-binding site (e.g., phenylquinoline scaffold) [7]. In our view, the “prodrugging” of the  $[\text{Cp}^*\text{Rh}]^{2+}$  scaffold into the cancer cells could represent a paradigm change since one can take advantage of Tyr conjugation selectivity to hit the protein substrates of PKs, and blocking the associated kinase-dependent pathways.

In analogy with CP, whose effective reactive species is obtained after aquation reaction, we propose that the  $[\text{Cp}^*\text{Rh}(\text{H}_2\text{O})_3]^{2+}$  complex could be in principle formed in the target biological compartment, i.e., the tumor tissue, by the hydrolysis of a precursor complex. Indeed, we envision that conjugated  $[\text{Cp}^*\text{Rh}(\eta^6\text{-Y})]^{2+}$  complexes, bearing aromatic scaffolds (Y) that could be released to restore the active tris-aquo complex in the biological environment, may act as prodrugs. In this view, Y should be properly designed to enhance the rate and the thermodynamics of the aquation reaction, and possibly favor the tissue selectivity with less toxic effects. Indeed, Rh(III) complexes containing polypyridyl ligands (Y) demonstrated potent antitumor activity



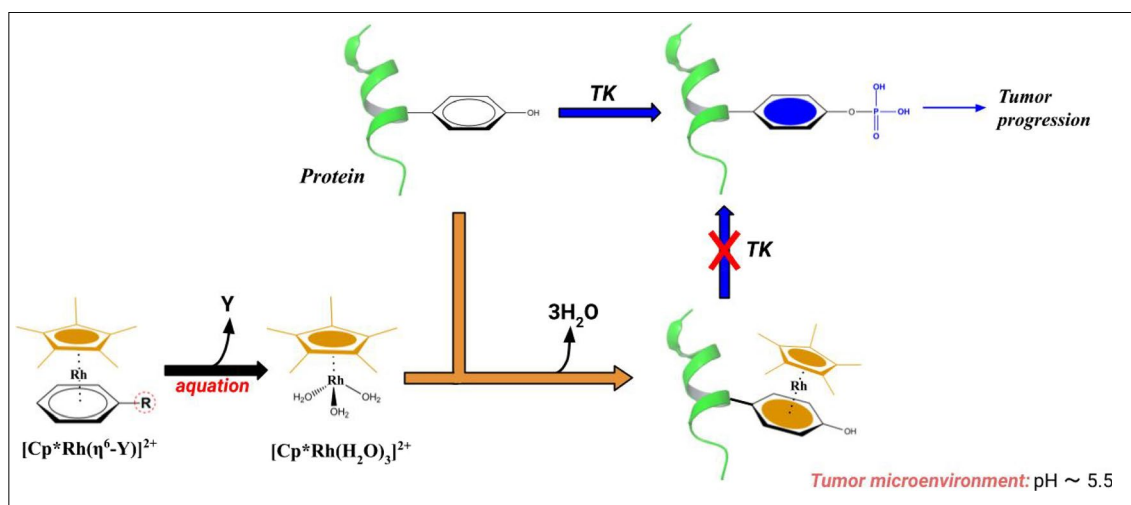


**Fig. 9** Schematic representation of possible antitumor action of  $[\text{Cp}^*\text{Rh}(\text{H}_2\text{O})_3]^{2+}$  inhibiting the phosphorylation of Tyr residue by means of a Tyr kinase enzyme

in vitro but their high toxicity impeded their application as drugs [57].

As shown in Fig. 9, after aquation reaction, the restored reactive species  $[\text{Cp}^*\text{Rh}(\text{H}_2\text{O})_3]^{2+}$ , interacts with the Tyr side chain of the protein enhanced by acid pH of the tumor microenvironment, and the formed  $[\text{Cp}^*\text{Rh}(\text{Tyr})]^{2+}$  complex impedes the Tyr post-translational modification that potentially block the tumor progression.

Within the same paradigm, other Tyr post-translational modifications may also be hampered by the in cellula  $\text{Cp}^*\text{Rh}(\text{III})$ -conjugation. For instance, the Tyr sulfation, involved in the tuning of protein–protein interactions affecting the leukocyte adhesion, hemostasis and chemokine signaling processes [58], may potentially be affected by the Tyr-conjugation with  $[\text{Cp}^*\text{Rh}]^{2+}$  and lead to innovative approaches, based on the disruption of PPIs, to treat related pathologies.

## Conclusion

The cationic complex  $[\text{Cp}^*\text{Rh}(\text{H}_2\text{O})_3]^{2+}$  has been demonstrated to react selectively with the phenolic side chain of Tyr, even in the presence of other aromatic a.a. side chains, such as Phe and Trp [17–19].

In this work, to deepen and clarify the mechanistic aspects of this high chemoselectivity, we studied in detail the conjugation of  $[\text{Cp}^*\text{Rh}(\text{H}_2\text{O})_3]^{2+}$  with three small molecules, **pC**, **3MI**, and **T**, mimetic of Tyr, Trp, and Phe side chains, respectively, by using the combined MTD/FMO3 and MD/FMO3 approaches.

Preliminary DFT calculations confirmed the highest stability of the  $[\text{Cp}^*\text{Rh}(\text{pC})]^{2+}$  complex compared with

$[\text{Cp}^*\text{Rh}(\text{3MI})]^{2+}$  and  $[\text{Cp}^*\text{Rh}(\text{T})]^{2+}$  and therefore the high selectivity for the Tyr side chain. The simulation of the formation of either the  $\text{Cp}^*\text{Rh}(\text{III})$ -conjugates or the non-covalent (aromatic scaffold)-- $[\text{Cp}^*\text{Rh}(\text{H}_2\text{O})_3]^{2+}$  encounter complexes were carried on via MTD or MD calculations at the tight-binding DFT level of theory.

The FMO analyses of the MTD and MD trajectories suggested that the higher selectivity for Tyr compared to Phe and Trp side chains might be related to the multifacet role played by the phenol OH group:

- The +M effect of the OH function increases the electron density on the phenol ring, strengthening the  $\eta^6$ -coordination in the final  $[\text{Cp}^*\text{Rh}(\text{pC})]^{2+}$  complex. Our calculations also showed that such an effect is significantly enhanced by the H bond with solvation water which polarizes the phenolic O-H bond increasing the partial negative charge on the O atom.
- At variance of **3MI** and **T** side chains, the phenolic OH group can act also as H bond acceptor thus establishing more effective H bond interactions with the aquo ligands of  $[\text{Cp}^*\text{Rh}(\text{H}_2\text{O})_3]^{2+}$  complex. These interactions probably favor the configurations of the non-covalent  $[\text{Cp}^*\text{Rh}(\text{H}_2\text{O})_3]^{2+}$  phenol EC amenable to the formation of the corresponding  $\eta^6$ -complex, and therefore increasing the reaction rate.

Interestingly, the analysis of MTD trajectories also showed that not only the formation of  $\eta^6$ -complexes proceeds via the interception of  $\eta^2$  and  $\eta^4$  intermediates, as previously found [19], but the **pC** compared to **T** and **3MI** demonstrated the most stable  $\eta^6$ -coordination. On the other hand, the MTD trajectories also unveiled the  $\eta$ -complexes,

mostly  $\eta^2$  and  $\eta^6$ , and the non-covalent EC coexist and showed that the aquation of  $[\text{Cp}^*\text{Rh}(\eta^6\text{-Y})]^{2+}$  complexes with  $\text{Y}=\text{aromatic scaffold}$ , is theoretically possible.

On the basis of abovementioned mechanistic aspects, we speculate that  $[\text{Cp}^*\text{Rh}(\eta^6\text{-Y})]^{2+}$  complexes could be employed as prodrugs of the  $[\text{Cp}^*\text{Rh}]^{2+}$  to afford the chemoselective  $\text{Cp}^*\text{Rh(III)}$ -conjugation of the Tyr side chains in cellula. In particular, we envision that newly designed  $[\text{Cp}^*\text{Rh}(\eta^6\text{-Y})]^{2+}$  complexes can be employed to target the Tyr residues involved in biological/pathological processes, such as Tyr-kinase enzyme activity and protein–protein interactions.

Therefore, our results might contribute to extend the knowledge of the mechanism underlining the Tyr chemoselective conjugation with the  $[\text{Cp}^*\text{Rh}(\text{H}_2\text{O})_3]^{2+}$  complex and inspire the design of a new class of  $[\text{Cp}^*\text{Rh}]^{2+}$ -based metallodrugs.

**Supplementary Information** The online version contains supplementary material available at <https://doi.org/10.1007/s00894-023-05794-z>.

**Author contributions** Conceptualization: RP; formal analysis and investigation: RP; writing—original draft preparation: RP; writing—review and editing: AM, RP; supervision: AM. All authors read and approved the final manuscript.

**Funding** Open access funding provided by Università degli Studi G. D'Annunzio Chieti Pescara within the CRUI-CARE Agreement.

**Data availability** The 3D coordinates of the optimized structures, obtained by sampling each 1 ps of the **EC1**, **EC2**, and **EC3** trajectories (MTD and MD calculations) and used as input geometries for FMO3 calculations, are available in the xyz file format at the following link <https://doi.org/10.5281/zenodo.8417065>.

## Declarations

**Ethical approval** Not applicable on this work.

**Consent for publication** All authors have read and understood the publishing policy, and this manuscript is submitted in accordance with this policy.

**Competing interests** The authors declare no competing interests.

**Open Access** This article is licensed under a Creative Commons Attribution 4.0 International License, which permits use, sharing, adaptation, distribution and reproduction in any medium or format, as long as you give appropriate credit to the original author(s) and the source, provide a link to the Creative Commons licence, and indicate if changes were made. The images or other third party material in this article are included in the article's Creative Commons licence, unless indicated otherwise in a credit line to the material. If material is not included in the article's Creative Commons licence and your intended use is not permitted by statutory regulation or exceeds the permitted use, you will need to obtain permission directly from the copyright holder. To view a copy of this licence, visit <http://creativecommons.org/licenses/by/4.0/>.

## References

- Rosenberg B, Vancamp L, Trosko JE, Mansour VH (1969) Platinum compounds: a new class of potent antitumour agents. *Nature* 222:385–386
- Cohen SM, Lippard SJ (2001) Cisplatin: from DNA damage to cancer chemotherapy. *Prog Nucleic Acid Res Mol Biol* 67:93–130
- Brown A, Kumar S, Tchounwou PB (2019) Cisplatin-based chemotherapy of human cancers. *J Cancer Sci Ther* 11(4):97
- Galluzzi L, Senovilla L, Vitale I, Michels J, Martins I, Kepp O, Castedo M, Kroemer G (2012) Molecular mechanisms of cisplatin resistance. *Oncogene* 31:1869–1883
- Pinzani V, Bressolle F, Haug JJ, Galtier M, Blayac JP, Balmès P (1994) Cisplatin-induced renal toxicity and toxicity-modulating strategies: a review. *Cancer Chemother Pharmacol* 35:1–9. <https://doi.org/10.1007/BF00686277>
- Ott I, Gust R (2007) Non platinum metal complexes as anti-cancer drugs. *Arch Pharm Pharm Med Chem* 340:117–126. <https://doi.org/10.1002/ardp.200600151>
- Leung CH, Zhong HJ, Chan DSH, Ma DL (2013) Bioactive iridium and rhodium complexes as therapeutic agents. *Coord Chem Rev* 257:1764–1776
- Fricker SP (2007) Metal based drugs: from serendipity to design. *Dalton Trans* 2007:4903–4917. <https://doi.org/10.1039/B705551J>
- Sohrabi M, Saeedi M, Larijani B, Mahdavi M (2021) Recent advances in biological activities of rhodium complexes: their applications in drug discovery research. *Eur J Med Chem* 216:113308
- Ma DL, He HZ, Leung KH, Chan DSH, Leung CH (2013) Bioactive luminescent transition-metal complexes for biomedical applications. *Angew Chem Int Ed* 52:7666–7682
- Schmidlehner M, Flocke LS, Roller A, Hejl M, Jakupec MA, Kandlioller W, Keppler BK (2016) Cytotoxicity and preliminary mode of action studies of novel 2-aryl-4-thiopyrone-based organometallics. *Dalton Trans* 45:724
- Ma DL, Wang M, Mao Z, Yang C, Ng CT, Leung CH (2016) Rhodium complexes as therapeutic agents. *Dalton Trans* 45:2762
- Blakemore JD, Hernandez ES, Sattler W, Hunter BM, Henling LM, Brunshwig BS, Gray HB (2014) Pentamethylcyclopentadienyl rhodium complexes. *Polyhedron* 84:14–18
- Hyster TK, Knoerr L, Ward TR, Rovis T (2012) Biotinylated Rh(III) complexes in engineered streptavidin for accelerated asymmetric C–H activation. *Science* 338:500
- Fish RH (2019) 1,4-NADH biomimetic co-factors with horse liver alcohol dehydrogenase (HLADH), utilizing  $[\text{Cp}^*\text{Rh}(\text{bpy})\text{H}](\text{OTf})$  for co-factor regeneration, do in fact, produce chiral alcohols from reactions with achiral ketones. *Catalysts* 9(6):562. <https://doi.org/10.3390/catal9060562>
- Markham J, Liang J, Levina A, Mak R, Johannessen B, Kappen P, Glover CJ, Lai B, Vogt S, Lay PA (2017) (Pentamethylcyclopentadienato)rhodium complexes for delivery of the curcumin anticancer drug. *Eur J Inorg Chem* 1812–1823. <https://doi.org/10.1002/ejic.201601331>
- Albada HB, Wieberneit F, Dijkgraaf I, Harvey JH, Whistler JL, Stoll R, Metzler-Nolte N, Fish RH (2012) The chemoselective reactions of tyrosine containing G-protein-coupled receptor peptides with  $[\text{Cp}^*\text{Rh}(\text{H}_2\text{O})_3](\text{OTf})_2$ , including 2D NMR structures and the biological consequences. *J Am Chem Soc* 134(25):10321–10324
- Wieberneit F, Korste A, Albada HB, Metzler-Noltes N, Stoll R (2013) Structural and biological implications of the binding of Leu-enkephalin, and its metal derivative to opioid receptors. *Dalton Trans* 42:9799

19. Paciotti R, Fish RH, Marrone A (2022) MD-DFT computational studies on the mechanistic and conformational parameters for the chemoselective tyrosine residue reactions of G-protein-coupled receptor peptides with  $[\text{Cp}^*\text{Rh}(\text{H}_2\text{O})_3](\text{OTf})_2$  in water to form their  $[(\eta^6\text{-Cp}^*\text{Rh-Tyr}\#)\text{-GPCR peptide}]^{2+}$  complexes: noncovalent H-bonding interactions, molecular orbital analysis, thermodynamics, and lowest energy conformations. *Organometallics* 41(16):2252–2267. <https://doi.org/10.1021/acs.organomet.2c00259>
20. Barducci A, Bonomi M, Parrinello M (2011) Metadynamics. *WIREs Comput Mol Sci* 1:826–843. <https://doi.org/10.1002/wcms.31>
21. Kitaura K, Ikeo E, Asada T, Nakano T, Uebayasi M (1999) Fragment molecular orbital method: an approximate computational method for large molecules. *Chem Phys Lett* 313:701–706
22. Steinmann C, Fedorov DG, Jensen JH (2010) Effective fragment molecular orbital method: a merger of the effective fragment potential and fragment molecular orbital methods. *J Phys Chem A* 114(33):8705–8712. <https://doi.org/10.1021/jp101498m>
23. Fedorov DG, Kitaura K (2007) Pair interaction energy decomposition analysis. *J Comput Chem* 28:222–237. <https://doi.org/10.1002/jcc.20496>
24. Fedorov DG, Kitaura K (2012) Energy decomposition analysis in solution based on the fragment molecular orbital method. *J Phys Chem A* 116:704–719. <https://doi.org/10.1021/jp209579w>
25. Paciotti R, Corinti D, Maître P, Coletti C, Re N, Chiavarino B, Crestoni ME, Fornarini S (2021) From preassociation to chelation: a survey of cisplatin interaction with methionine at molecular level by IR ion spectroscopy and computations. *J Am Soc Mass Spectrom* 32(8):2206–2217. <https://doi.org/10.1021/jasms.1c00152>
26. Corinti D, Paciotti R, Re N, Coletti C, Chiavarino B, Crestoni ME, Fornarini S (2020) Binding motifs of cisplatin interaction with simple biomolecules and aminoacid targets probed by IR ion spectroscopy. *Pure Appl Chem* 92:3–13
27. Corinti D, Paciotti R, Coletti C, Re N, Chiavarino B, Crestoni ME, Fornarini S (2022) Elusive intermediates in cisplatin reaction with target amino acids: platinum(II)-cysteine complexes assayed by IR ion spectroscopy and DFT calculations. *J Inorg Biochem* 237:112017. <https://doi.org/10.1016/j.jinorgbio.2022.112017>
28. Frisch MJ, Trucks GW, Schlegel HB, Scuseria GE, Robb MA, Cheeseman JR, Scalmani G, Barone V, Mennucci B, Petersson GA (2009) Gaussian 09, Revision D.01. Gaussian Inc, Wallingford, CT, USA
29. Grimme S (2019) Exploration of chemical compound, conformer, and reaction space with meta-dynamics simulations based on tight-binding quantum chemical calculations. *J Chem Theory Comput* 15:2847–2862. <https://doi.org/10.1021/acs.jctc.9b00143>
30. Bannwarth C, Ehlert S, Grimme S (2019) GFN2-xTB—an accurate and broadly parametrized self-consistent tight-binding quantum chemical method with multipole electrostatics and density-dependent dispersion contributions. *J Chem Theory Comput* 15(3):1652–1671
31. Bannwarth C, Caldeweyher E, Ehlert S, Hansen A, Pracht P, Seibert J, Spicher S, Grimme S (2021) Extended tight-binding quantum chemistry methods. *WIREs Comput Mol Sci* 11:e01493. <https://doi.org/10.1002/wcms.1493>
32. Fedorov DG, Kitaura K (2006) The three-body fragment molecular orbital method for accurate calculations of large systems. *Chem Phys Lett* 433:182–187. <https://doi.org/10.1016/j.cplett.2006.10.052>
33. Storchi L, Paciotti R, Re N, Marrone A (2015) Investigation of the molecular similarity in closely related protein systems: the PrP case study. *Proteins* 83:1751–1765. <https://doi.org/10.1002/prot.24836>
34. Ishikawa T, Ishikura T, Kuwata K (2009) Theoretical study of the prion protein based on the fragment molecular orbital method. *J Comput Chem* 30:2594–2601. <https://doi.org/10.1002/jcc.21265>
35. Paciotti R, Storchi L, Marrone A (2019) An insight of early PrPE200K aggregation by combined molecular dynamics/fragment molecular orbital approaches. *Proteins* 87:51–61. <https://doi.org/10.1002/prot.25621>
36. Paciotti R, Storchi L, Marrone A (2022) Homodimeric complexes of the 90–231 human prion: a multilayered computational study based on FMO/GRID-DRY approach. *J Mol Model* 28:241. <https://doi.org/10.1007/s00894-022-05244-2>
37. Kurisaki I, Fukuzawa K, Komeiji Y, Mochizuki Y, Nakano T, Imada J, Chmielewski A, Rothstein SM, Watanabe H, Tanaka S (2007) Visualization analysis of inter-fragment interaction energies of CRP–cAMP–DNA complex based on the fragment molecular orbital method. *Biophys Chem* 130:1–9. <https://doi.org/10.1016/j.bpc.2007.06.011>
38. Paciotti R, Agamennone M, Coletti C, Storchi L (2020) Characterization of PD-L1 binding sites by a combined FMO/GRID-DRY approach. *J Comput Aided Mol Des* 34:897–914. <https://doi.org/10.1007/s10822-020-00306-0>
39. Guareschi R, Lukac I, Gilbert IH, Zuccotto F (2023) SophosQM: accurate binding affinity prediction in compound optimization. *ACS Omega* 8:15083–15098. <https://doi.org/10.1021/acsomega.2c08132>
40. Corinti D, Paciotti R, Coletti C, Re N, Chiavarino B, Frison G, Crestoni ME, Fornarini S (2023) IRMPD spectroscopy and quantum-chemical simulations of the reaction products of cisplatin with the dipeptide CysGly. *J Inorg Biochem* 247:112342. <https://doi.org/10.1016/j.jinorgbio.2023.112342>
41. Ishikawa T, Kuwata K (2009) Fragment molecular orbital calculation using the RI-MP2 method. *Chem Phys Lett* 474:195–198. <https://doi.org/10.1016/j.cplett.2009.04.045>
42. Mori H, Ueno-Noto K, Osanai Y, Noro T, Fujiwara T, Klobukowski M, Miyoshi E (2009) Revised model core potentials for third-row transition–metal atoms from Lu to Hg. *Chem Phys Lett* 476:317–322. <https://doi.org/10.1016/j.cplett.2009.06.019>
43. Floris FM, Tomasi J, Ahuir JP (1991) Dispersion and repulsion contributions to the solvation energy: refinements to a simple computational model in the continuum approximation. *J Comput Chem* 12:784–791. <https://doi.org/10.1002/jcc.540120703>
44. Si D, Li H (2009) Heterogeneous conductor like solvation model. *J Chem Phys* 131:044123. <https://doi.org/10.1063/1.3187527>
45. Fedorov DG (2019) Solvent screening in zwitterions analyzed with the fragment molecular orbital method. *J Chem Theory Comput* 15:5404–5416. <https://doi.org/10.1021/acs.jctc.9b00715>
46. Paciotti R, Coletti C, Marrone A, Re N (2022) The FMO2 analysis of the ligand-receptor binding energy: the biscarbene-gold(I)/DNA G-quadruplex case study. *J Comput Aided Mol Des* 36:851–866. <https://doi.org/10.1007/s10822-022-00484-z>
47. Paciotti R, Marrone A, Coletti C, Re N (2023) Improving the accuracy of the FMO binding affinity prediction of ligand-receptor complexes containing metals. *J Comput Aided Mol Des*. <https://doi.org/10.1007/s10822-023-00532-2>
48. Fedorov DG, Slipchenko LV, Kitaura K (2010) Systematic study of the embedding potential description in the fragment molecular orbital method. *J Phys Chem A* 114:8742–8753. <https://doi.org/10.1021/jp101724p>
49. Fedorov DG (2020) Three-body energy decomposition analysis based on the fragment molecular orbital method. *J Phys Chem A* 124:4956–4971. <https://doi.org/10.1021/acs.jpca.0c03085>
50. Ozawa M, Ozawa T, Ueda K (2017) Application of the fragment molecular orbital method analysis to fragment-based drug discovery of BET (bromodomain and extra-terminal proteins) inhibitors. *J Mol Graph Model* 74:73–82

51. Barca GMJ, Bertoni C, Carrington L, Datta D, De Silva N, Deustua JE, Fedorov DG, Gour JR, Gunina AO, Guidez E, Harville T, Irle S, Ivanic J, Kowalski K, Leang SS, Li H, Li W, Lutz JJ, Magoulas I et al (2020) Recent developments in the general atomic and molecular electronic structure system. *J Chem Phys* 152:154102. <https://doi.org/10.1063/5.0005188>
52. Mazanetz MP, Ichihara O, Law RJ, Whittaker M (2011) Prediction of cyclin-dependent kinase 2 inhibitor potency using the fragment molecular orbital method. *Aust J Chem* 3(2):1–15. <https://doi.org/10.1186/1758-2946-3-2>
53. Efremenko I, Fish RH (2015) Quantum chemical and molecular docking studies of  $[(\eta^6\text{-Cp}^*\text{Rh-Tyr}^1)\text{-Leu-enkephalin}]^{2+}$  to G-protein-coupled  $\mu$ -,  $\delta$ -, and  $\kappa$ -opioid receptors, and comparisons to the neuropeptide,  $[\text{Tyr}^1]\text{-Leu-enkephalin}$ : conformations, non-covalent amino acid binding sites, binding energies, electronic factors, and receptor distortion forces. *Organometallics* 34:4117
54. Fedorov DG, Nakamura T (2022) Free energy decomposition analysis based on the fragment molecular orbital method. *J Phys Chem Lett* 13(6):1596–1601. <https://doi.org/10.1021/acs.jpcclett.2c00040>
55. Hunter T (2009) Tyrosine phosphorylation: thirty years and counting. *COCEBI* 21:140–114
56. Paul MK, Mukhopadhyay AK (2004) Tyrosine kinase - role and significance in cancer. *Int J Med Sci* 1(2):101–115
57. Geldmacher Y, Oleszak M, Sheldrick WS (2012) Rhodium(III) and iridium(III) complexes as anticancer agents. *Inorg Chim Acta* 393:84–102
58. Kehoe JW, Bertozzi CR (2000) Tyrosine sulfation: a modulator of extracellular protein–protein interactions. *Chem Biol* 7(3):57–61. [https://doi.org/10.1016/S1074-5521\(00\)00093-4](https://doi.org/10.1016/S1074-5521(00)00093-4)

**Publisher's Note** Springer Nature remains neutral with regard to jurisdictional claims in published maps and institutional affiliations.